Nucleation process in asymmetric hot nuclear matter

D. P. Menezes* and C. Providência

Centro de Física Teórica, Departamento de Física, Universidade de Coimbra, Coimbra 3000, Portugal
(Received 25 September 1998; published 21 July 1999)

An extended version of the nonlinear Walecka model, with ρ mesons and electromagnetic field is used to investigate the possibility of phase transitions in hot (warm) nuclear matter, giving rise to droplet formation. Surface properties of asymmetric nuclear matter as the droplet surface energy and its thickness are also examined. The effects of the Coulomb interaction are discussed. [S0556-2813(99)01808-7]

I. INTRODUCTION

In heavy-ion collisions, part of the hot nuclear matter produced can be described in terms of hadrons. The formation of highly excited composed nuclei in equilibrium with a gas of evaporated particles can be interpreted in the framework of hydrodynamics as two coexisting phases of nuclear matter, a liquid and a gas phase [1]. During these reactions, phase transitions may occur depending on the temperature and densities involved [2–4]. The investigation of asymmetric nuclear matter is also of particular interest for problems in astrophysics. In fact, neutron-star matter at densities between 0.03 fm^{-3} and nuclear matter density (0.17 fm^{-3}) consists of neutron-rich nuclei immersed in a gas of neutrons [5]. The size of the nuclei is determined by a competition between the surface energy and the Coulomb interaction. The use of thermodynamical concepts in the study of possible phase transitions in the above problems is done with the underlying assumption that the time required for thermalization and chemical equilibrium is short.

Hot nuclei, liquid-gas phase transitions and droplet formation in nuclear reactions as well as the surface properties of nuclear matter have already been extensively discussed in the literature in the context of nonrelativistic models, namely within the framework of the Hartree-Fock (HF), Thomas-Fermi (TF) and extended-Thomas-Fermi approximations (ETF) [1,6–10]. In particular, in [10] it is shown that the semiclassical TF approximation scheme is reasonably accurate at any temperature.

Within the framework of relativistic models phase transitions in hot (warm) nuclear matter have also been investigated in infinite matter by imposing constant mesonic fields [2], at zero temperature for symmetric semi-infinite nuclear matter [11], at finite temperature for symmetric matter in the linear Walecka model [3,12] and also in its nonlinear form for symmetric and asymmetric matter [13]. Surface properties of asymmetric semi-infinite nuclear matter have been investigated at zero temperature in [14] and [15] by a semiclassical approach. In most of the above mentioned papers in which temperature effects have been taken into account, the finite temperature version of the liquid drop model is used in the investigation of the surface properties of the arising droplet.

The importance of the Coulomb interaction in nuclear systems cannot be denied. Although its *role* has already been investigated in the framework of some of the non-relativistic works discussed above, the electromagnetic field has been systematically neglected in relativistic models. In a previous work [16] we have investigated droplet formation in a vapor system at zero temperature in the framework of the relativistic Walecka model with nonlinear terms (NLWM), which is known to describe adequately the bulk properties of nuclear matter. We have included the Coulomb interaction and worked in the Thomas-Fermi approximation. In the present work, we study the possibility of droplet formation in a vapor system at finite temperature within the same framework. We determine the conditions for phase coexistence in a multicomponent system by building the binodals for two temperatures and two parametrizations of the nonlinear Walecka model. These values determine the initial and boundary conditions which are used in solving numerically the coupled equations of motion obtained in the Thomas-Fermi approximation at finite temperature. The properties of the droplets such as the surface energy and thickness, the neutron skin thickness and the proton fraction are calculated. These properties are important, for instance, in the study of the phase boundary between the liquid matter in the interior of a neutron star and the matter that comprises its crust. Also, in energetic collisions of two heavy ions the evolution of the system can go through a process of nucleation during which the system separates into droplets and vapor or bubbles and liquid.

In Sec. II we obtain the equations of motion in the static case. The thermodynamical potential in the framework of the Thomas-Fermi approximation is calculated in Sec. III. In Sec. IV the two-phase coexistence is discussed and in Sec. V we present the numerical results. Finally, in the last section some conclusions are drawn.

II. EXTENDED NONLINEAR WALECKA MODEL

In what follows we describe the equation of state of asymmetric matter within the framework of the relativistic nonlinear Walecka model [17,18] with the inclusion of ρ-mesons and the electromagnetic field. The self interaction terms of the scalar meson were shown to be necessary in order to adequately describe nuclear properties [17]. Both the ρ me-

---

*Permanent address: Depto. de Física, CFM, Universidade Federal de Santa Catarina, Florianópolis-SC-CP. 476-CEP 88.040-900, Brazil.

60 024313-1

TABLE I. Sets of parameters used in this work. All masses are given in MeV. The (∗) is a reminder that the authors of [2] have not given the scalar meson mass used in their parametrization.

Force	[Ref.]	C_s^2	C_v^2	C_ρ^2	$\kappa/M \times 10^{-3}$	$\lambda \times 10^{-3}$	ξ	M	m_s	m_v	m_ρ
MS	[1]	374.770	260.570	106.91	3.0809×10^3	8.106×10^3	0.02364	939	550.00∗	783.00	770.00
NL1	[12]	373.176	245.458	149.67	$2\ g_s^3$ $\ 2.4578$	$-6\ g_s^4$ $\ 3.4334$	0.0	938	492.25	795.36	763.00

son and photons are incorporated to account, respectively, for the neutron excess in heavy nuclei and the electromagnetic interaction between the protons [18]. In our Lagrangian the π-meson field amplitude is not considered since we are not interested in pion-condensed states and hence, under the approximation we use here, all pion contributions vanish. Although we also have in mind the description of neutron star crusts, the pionic degrees of freedom are not considered because their *role* only becomes important for matter much denser than the one investigated in the present work.

In this model the nucleons are coupled to neutral scalar ϕ, isoscalar-vector V^μ, isovector-vector $\vec{b}^\mu$ meson fields and the electromagnetic field A^μ. The Lagrangian density reads

$$\mathcal{L} = \bar{\psi}\left[\gamma_\mu\left(i\partial^\mu - g_v V^\mu - \frac{g_\rho}{2}\vec{\tau}\cdot\vec{b}^\mu - eA^\mu\frac{(1+\tau_3)}{2} \right) \right.$$
$$\left. - (M - g_s\phi) \right]\psi + \frac{1}{2}(\partial_\mu\phi\partial^\mu\phi - m_s^2\phi^2) - \frac{1}{3!}\kappa\phi^3$$
$$- \frac{1}{4!}\lambda\phi^4 - \frac{1}{4}\Omega_{\mu\nu}\Omega^{\mu\nu} + \frac{1}{2}m_v^2 V_\mu V^\mu + \frac{1}{4!}\xi g_v^4(V_\mu V^\mu)^2$$
$$- \frac{1}{4}\vec{B}_{\mu\nu}\cdot\vec{B}^{\mu\nu} + \frac{1}{2}m_\rho^2\vec{b}_\mu\cdot\vec{b}^\mu - \frac{1}{4}F_{\mu\nu}F^{\mu\nu}, \tag{1}$$

where

$$\Omega_{\mu\nu} = \partial_\mu V_\nu - \partial_\nu V_\mu, \tag{2}$$

$$\vec{B}_{\mu\nu} = \partial_\mu\vec{b}_\nu - \partial_\nu\vec{b}_\mu - g_\rho(\vec{b}_\mu \times \vec{b}_\nu), \tag{3}$$

and

$$F_{\mu\nu} = \partial_\mu A_\nu - \partial_\nu A_\mu. \tag{4}$$

The model comprises the following parameters: three coupling constants g_s, g_v, and g_ρ of the mesons to the nucleons, the nucleon mass M, the masses of the mesons m_s, m_v, m_ρ, the electromagnetic coupling constant $e = \sqrt{4\pi/137}$ and the self-interacting coupling constants κ, λ, and ξ. We have used two sets of constants, respectively identified as MS taken from [2] and as NL1 taken from [23], with $C_i^2 = g_i^2 M^2/m_i^2$, $i = s$, v, ρ, and they are displayed in Table I. All meson masses must be specified along with the coupling constants. It is true that only the rations of couplings to the masses are necessary in infinite matter in the *linear* Walecka model. When nonlinear terms are included, the statement loses its validity.

From the Euler-Lagrange formalism, we obtain the coupled equations of motion for the scalar, isoscalar-vector, isovector-vector, electromagnetic and nucleon fields, respectively given by

$$(\partial_t^2 - \nabla^2 + m_s^2)\phi = g_s\rho_s - \frac{\kappa}{2}\phi^2 - \frac{\lambda}{6}\phi^3, \tag{5}$$

$$(\partial_t^2 - \nabla^2 + m_v^2)V^\mu = g_v j^\mu - \frac{\xi}{6}g_v^4(V^\mu V_\mu)V^\mu, \tag{6}$$

$$(\partial_t^2 - \nabla^2 + m_\rho^2)\vec{b}^\mu = \frac{g_\rho}{2}\vec{j}^\mu + \frac{g_\rho}{2}(\vec{b}_\nu \times \vec{B}^{\nu\mu}) + g_\rho\partial_\nu(\vec{b}^\nu \times \vec{b}^\mu), \tag{7}$$

$$(\partial_t^2 - \nabla^2)A^\mu = \frac{e}{2}j_{em}^\mu, \tag{8}$$

and

$$i\partial_t\psi = \left[\boldsymbol{\alpha}\cdot\left(-i\boldsymbol{\nabla} - g_v\mathbf{V} - \frac{g_\rho}{2}\tau_3\mathbf{b} - e\frac{(1+\tau_3)}{2}\mathbf{A} \right) \right.$$
$$+ \beta(M - g_s\phi) + g_v V^0 + \frac{g_\rho}{2}\tau_3 b^0$$
$$\left. + e\frac{(1+\tau_3)}{2}A^0 \right]\psi, \tag{9}$$

where the scalar density ρ_s and the baryonic current densities are defined as

$$\rho_s = \langle\bar{\psi}\psi\rangle,$$

$$j^\mu = \langle\bar{\psi}\gamma^\mu\psi\rangle,$$

$$\vec{j}^\mu = \langle\bar{\psi}\gamma^\mu\vec{\tau}\psi\rangle,$$

$$j_{em}^\mu = \left\langle \bar{\psi}\gamma^\mu\left(\frac{1+\tau_3}{2}\right)\psi \right\rangle$$

and $b_3^\mu \equiv (b^0, \mathbf{b})$. In the static case there are no currents in the droplet and the spatial vector components $\mathbf{V}$, $\mathbf{b}$, and $\mathbf{A}$ are zero. Therefore, the equations of motion become

$$\nabla^2\phi = m_s^2\phi + \frac{1}{2}\kappa\phi^2 + \frac{1}{3!}\lambda\phi^3 - g_s\rho_s, \tag{10}$$

$$\nabla^2 V_0 = m_v^2 V_0 + \frac{1}{3!}\xi g_v^4 V_0^3 - g_v\rho_B, \tag{11}$$

$$\nabla^2 b_0 = m_\rho^2 b_0 - \frac{g_\rho}{2}\rho_3, \qquad (12)$$

$$\nabla^2 A_0 = -e\rho_p, \qquad (13)$$

where $\rho_B = \rho_p + \rho_n$ and $\rho_3 = \rho_p - \rho_n$ are the baryonic densities, and ρ_p and ρ_n are the proton and neutron densities.

III. THE THOMAS-FERMI APPROXIMATION

The present work is based on the semiclassical Thomas-Fermi approximation. In this approach the energy of the nuclear system with particles and antiparticles, described respectively by the one-body phase-space distribution functions $n_+(\mathbf{r},\mathbf{p},t)$ and $n_-(\mathbf{r},\mathbf{p},t)$, at position $\mathbf{r}$ time t and with momentum $\mathbf{p}$

$$n_\pm(\mathbf{r},\mathbf{p},t) = \begin{pmatrix} n_{p\pm}(\mathbf{r},\mathbf{p},t) & 0 \\ 0 & n_{n\pm}(\mathbf{r},\mathbf{p},t) \end{pmatrix}, \qquad (14)$$

is (only the nuclear matter contribution and interaction terms)

$$E_N = \gamma \operatorname{Tr} \int \frac{d^3r\,d^3p}{(2\pi)^3}[n_+(\mathbf{r},\mathbf{p},t)\epsilon_+ + n_-(\mathbf{r},\mathbf{p},t)\epsilon_-], \qquad (15)$$

where

$$\epsilon_\pm = \begin{pmatrix} \epsilon_{p\pm} & 0 \\ 0 & \epsilon_{n\pm} \end{pmatrix},$$

$$\epsilon_{i\pm} = \sqrt{(\mathbf{p}\mp\mathcal{V}_i)^2 + (M - g_s\phi)^2} \pm \mathcal{V}_{i0}, \quad i = p,n,$$

with

$$\mathcal{V}_{p0} = g_v V_0 + \frac{g_\rho}{2}b_0 + eA_0, \quad \mathcal{V}_{n0} = g_v V_0 - \frac{g_\rho}{2}b_0,$$

$$\mathcal{V}_p = g_v \mathbf{V} + \frac{g_\rho}{2}\mathbf{b} + e\mathbf{A}, \quad \mathcal{V}_n = g_v \mathbf{V} - \frac{g_\rho}{2}\mathbf{b},$$

are the classical effective one-body Hamiltonian for particles $(+)$ and antiparticles $(-)$ since particles and antiparticles have opposite baryonic charge and $\gamma = 2$ refers to the spin multiplicity. We can also work with the distribution function for particles at position $\mathbf{r}$, instant t with momentum $\mathbf{p}$, $f_+(\mathbf{r},\mathbf{p},t) = n_+(\mathbf{r},\mathbf{p},t)$ and the distribution function for antiparticles at position $\mathbf{r}$, instant t with momentum $-\mathbf{p}$, $f_-(\mathbf{r},\mathbf{p},t) = n_-(\mathbf{r},-\mathbf{p},t)$ so that

$$E_N = \gamma \operatorname{Tr} \int \frac{d^3r\,d^3p}{(2\pi)^3}[f_+(\mathbf{r},\mathbf{p},t)h_+ - f_-(\mathbf{r},\mathbf{p},t)h_-],$$

where

$$h_\pm = \pm\epsilon_\pm(\mathbf{r},\pm\mathbf{p},t) = \begin{pmatrix} \pm\sqrt{(\mathbf{p}-\mathcal{V}_p)^2 + (M - g_s\phi)^2} + \mathcal{V}_{p0} & 0 \\ 0 & \pm\sqrt{(\mathbf{p}-\mathcal{V}_n)^2 + (M - g_s\phi)^2} + \mathcal{V}_{n0} \end{pmatrix}.$$

The classical entropy of a Fermi gas is given by

$$S = -\gamma \sum_{i=p,n}\int \frac{d^3r\,d^3p}{(2\pi)^3}\left(f_{i+}\ln\left(\frac{f_{i+}}{1-f_{i+}}\right) + \ln(1-f_{i+}) + (f_{i+}\leftrightarrow f_{i-})\right), \qquad (16)$$

and the thermodynamic potential is defined as

$$\Omega = E - TS - \sum_{i=p,n}\mu_i B_i, \qquad (17)$$

where B_p, B_n are, respectively, the proton and the neutron number:

$$B_i = \int d^3r\,\rho_i(\mathbf{r},t), \quad \rho_i = \gamma\int \frac{d^3p}{(2\pi)^3}(f_{i+} - f_{i-}), \quad i = p,n, \qquad (18)$$

μ_i is the chemical potential for particles of type i and T is the temperature. For a system in equilibrium, the distribution functions should be chosen to make the thermodynamic potential Ω stationary and hence

$$f_{i\pm}(\mathbf{r},\mathbf{p},t) = \frac{1}{1 + \exp[(\epsilon \mp \nu_i)/T]}, \quad i = p,n, \qquad (19)$$

where $\nu_i = \mu_i - \mathcal{V}_{i0}$ are the effective chemical potentials, $\epsilon = \sqrt{p^2 + M^{*2}}$ and $M^* = M - g_s\phi$ is the effective nucleon mass. In the static approximation $\mathcal{V}_\pm = 0$.

From the above expressions we get for Eq. (17)

$$\Omega = \gamma \operatorname{Tr} \int \frac{d^3 r\, d^3 p}{(2\pi)^3} [f_+(\mathbf{r},\mathbf{p},t)h_+ - f_-(\mathbf{r},\mathbf{p},t)h_-] + \frac{1}{2}\int d^3 r[(\nabla\phi)^2 - (\nabla V_0)^2 - (\nabla b_0)^2 - (\nabla A_0)^2]$$

$$+ \frac{1}{2}\int d^3 r\left[m_s^2\phi^2 + \frac{2}{3!}\kappa\phi^3 + \frac{2}{4!}\lambda\phi^4 - m_v^2 V_0^2 - \frac{2}{4!}\xi g_v^4 V_0^4 - m_\rho^2 b_0^2\right]$$

$$- \gamma T \sum_i \int d^3 r \frac{d^3 p}{(2\pi)^3}\left[\frac{h_{i+}}{T}f_{i+} - \frac{h_{i-}}{T}f_{i-} + \ln(1 + e^{-(\epsilon - \nu_i)/T}) + \ln(1 + e^{-(\epsilon + \nu_i)/T})\right]. \tag{20}$$

Equation (20) can then be written in the form

$$\Omega = \int d^3 r\left(\frac{1}{2}[(\nabla\phi)^2 - (\nabla V_0)^2 - (\nabla b_0)^2 - (\nabla A_0)^2] - V_{ef}\right),$$

with

$$V_{ef} = -\frac{1}{2}\left[m_s^2\phi^2 + \frac{2}{3!}\kappa\phi^3 + \frac{2}{4!}\lambda\phi^4 - m_v^2 V_0^2 \right.$$

$$\left. - \frac{2}{4!}\xi g_v^4 V_0^4 - m_\rho^2 b_0^2\right]$$

$$+ \gamma T \sum_i \int \frac{d^3 p}{(2\pi)^3}[\ln(1 + e^{-(\epsilon - \nu_i)/T})$$

$$+ \ln(1 + e^{-(\epsilon + \nu_i)/T})]. \tag{21}$$

The fields that minimize Ω satisfy the equations

$$\frac{\partial V_{ef}}{\partial\phi} = -m_s^2\phi - \frac{1}{2}\kappa\phi^2 - \frac{1}{3!}\lambda\phi^3 + g_s\rho_s, \tag{22}$$

$$\frac{\partial V_{ef}}{\partial V_0} = m_v^2 V_0 + \frac{1}{3!}\xi g_v^4 V_0^3 - g_v\rho_B, \tag{23}$$

$$\frac{\partial V_{ef}}{\partial b_0} = m_\rho^2 b_0 - \frac{g_\rho}{2}\rho_3, \tag{24}$$

$$\frac{\partial V_{ef}}{\partial A_0} = -e\rho_p, \tag{25}$$

where ρ_B, ρ_3 were defined at the end of Sec. II, ρ_p has been defined in Eq. (18) and

$$\rho_s = \gamma \sum_{i=p,n} \int \frac{d^3 p}{(2\pi)^3} \frac{M^*}{\epsilon}(f_{i+} + f_{i-}).$$

Comparing Eqs. (10)–(13) with Eqs. (22)–(25), we see that

$$\nabla^2\phi = \frac{d^2\phi}{dr^2} + \frac{2}{r}\frac{d\phi}{dr} = -\frac{\partial V_{ef}}{\partial\phi}, \tag{26}$$

$$\nabla^2 V_0 = \frac{d^2 V_0}{dr^2} + \frac{2}{r}\frac{dV_0}{dr} = \frac{\partial V_{ef}}{\partial V_0}, \tag{27}$$

$$\nabla^2 b_0 = \frac{d^2 b_0}{dr^2} + \frac{2}{r}\frac{db_0}{dr} = \frac{\partial V_{ef}}{\partial b_0}, \tag{28}$$

$$\nabla^2 A_0 = \frac{d^2 A_0}{dr^2} + \frac{2}{r}\frac{dA_0}{dr} = \frac{\partial V_{ef}}{\partial A_0}. \tag{29}$$

These coupled differential equations are solved numerically and all relevant quantities (e.g., effective mass, densities, pressure), which depend on the fields are calculated.

IV. TWO-PHASE COEXISTENCE

In order to obtain the initial conditions for the program which integrates the differential equations (26)–(29) we determine the conditions under which two distinct phases can coexist in infinite matter. In this case, the electromagnetic field is omitted. In the mean field approximation the meson fields are replaced by their expectation values [2,19,20],

$$\phi \equiv \langle\phi\rangle = \phi_0, \tag{30}$$

$$V^0 \equiv \langle V^0\rangle = V_0, \tag{31}$$

$$b^0 \equiv \langle b^0\rangle = b_0. \tag{32}$$

The substitution of the above expressions in Eqs. (10), (11), and (12) yields

$$\phi_0 = -\frac{\kappa}{2m_s^2}\phi_0^2 - \frac{\lambda}{6}\phi_0^3 + \frac{g_s}{m_s^2}\rho_s, \tag{33}$$

$$V_0 = -\frac{\xi g_v^4}{6m_v^2}V_0^3 + \frac{g_v}{m_v^2}\rho_B, \tag{34}$$

$$b_0 = \frac{g_\rho}{2m_\rho^2}\rho_3. \tag{35}$$

The thermodynamic quantities of interest are given in terms of the above meson fields. They are the energy density,
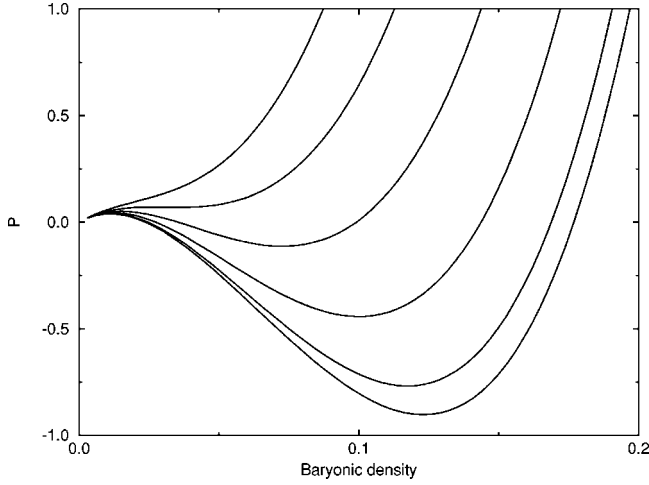
FIG. 1. The pressure in terms of the baryonic density is plotted for each proton fraction for the MS set of constants. From top to bottom we have $Y_p = 0, 0.1, 0.2, 0.3, 0.4, 0.5$. The temperature is $T = 7.5$ MeV. The pressure is given in MeV/fm^3 and the density in fm^{-3}.

$$\mathcal{E} = \frac{\gamma}{2\pi^2} \sum_{i=p,n} \int dp \, p^2 \sqrt{p^2 + M^{*2}} (f_{i+} + f_{i-}) + \frac{m_v^2}{2} V_0^2$$

$$+ \frac{\xi g_v^4}{8} V_0^4 + \frac{m_\rho^2}{2} b_0^2 + \frac{m_s^2}{2} \phi_0^2 + \frac{\kappa}{6} \phi_0^3 + \frac{\lambda}{24} \phi_0^4, \qquad (36)$$

the pressure,

$$P = \frac{\gamma}{6\pi^2} \sum_{i=p,n} \int dp \, \frac{p^4}{\sqrt{p^2 + M^{*2}}} (f_{i+} + f_{i-}) + \frac{m_v^2}{2} V_0^2$$

$$+ \frac{\xi g_v^4}{24} V_0^4 + \frac{m_\rho^2}{2} b_0^2 - \frac{m_s^2}{2} \phi_0^2 - \frac{\kappa}{6} \phi_0^3 - \frac{\lambda}{24} \phi_0^4, \qquad (37)$$

the entropy density,

$$\mathcal{S} = \frac{1}{T} (\mathcal{E} + P - \mu_p \rho_p - \mu_n \rho_n), \qquad (38)$$

and the proton fraction,

$$Y_p = \frac{\rho_p}{\rho_B}. \qquad (39)$$

A thorough study of the possibility of phase transitions in hot, asymmetric nuclear matter is done in [21] and [2]. In Fig. 1 we plot the pressure in terms of the baryonic density ρ_B for several proton fractions at $T = 7.5$ MeV obtained with the MS constants. Similar behaviors are found for $T = 5$ MeV and also with the NL1 constants.

We have made use of the geometrical construction [21] in order to obtain the chemical potentials in the two coexisting phases for each pressure of interest. As an example, we show μ_p and μ_n as function of the proton fractions in Fig. 2 again with the MS parametrization for $T = 7.5$ MeV and $P = 0.068$ MeV/fm^3.
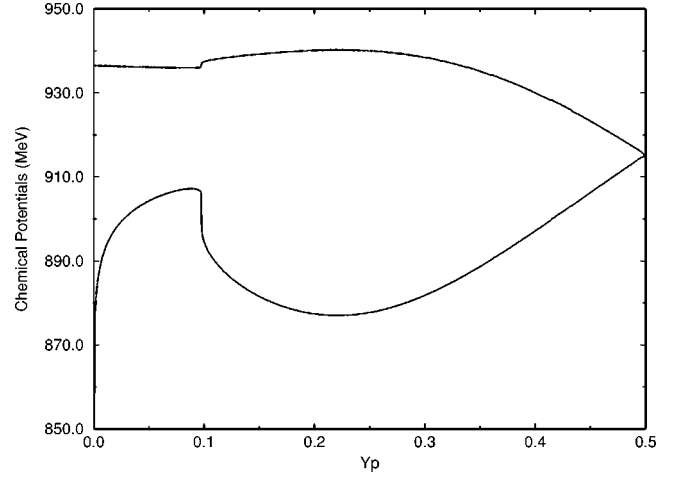

FIG. 2. The proton (lower curve) and the neutron (upper curve) chemical potentials are shown in function of the proton fraction for the pressure of 0.068 MeV/fm^3. Again this graph is plotted for MS constants and $T = 7.5$ MeV.

In a binary system we have

$$\left(\frac{\partial \mu_p}{\partial Y_p} \right)_{T,P} \geq 0 \quad \text{and} \quad \left(\frac{\partial \mu_n}{\partial Y_p} \right)_{T,P} \leq 0, \qquad (40)$$

known as diffusive stability, which reflects the fact that in a stable system, energy is required to change the proton concentration while pressure and temperature are kept constant. In order to obtain the binodal section which contains points under the same pressure for different proton fractions, we have used the conditions above and simultaneously solved the following equations:

$$P = P(\nu_p, \nu_n, M^*), \qquad (41)$$

$$P = P(\nu'_p, \nu'_n, M^{*'}), \qquad (42)$$

$$\mu_i(\nu_p, \nu_n, M^*) = \mu_i(\nu'_p, \nu'_n, M^{*'}), \quad i = p, n, \qquad (43)$$

$$m_s^2 \phi_0 + \frac{\kappa}{2} \phi_0^2 + \frac{\lambda}{6} \phi_0^3 = g_s \rho_s(\nu_p, \nu_n, M^*), \qquad (44)$$

and

$$m_s^2 \phi_0' + \frac{\kappa}{2} \phi_0'^2 + \frac{\lambda}{6} \phi_0'^3 = g_s \rho_s(\nu'_p, \nu'_n, M^{*'}). \qquad (45)$$

The binodal sections for the MS constants and temperatures equal to 5 and 7.5 MeV are plotted in Fig. 3. In Fig. 4 the binodal section for $T = 5$ MeV is shown for the NL1 set of parameters. For certain values of proton and neutron chemical potentials, the system may be at the same pressure with different densities and proton concentrations, which allows for the possibility of phase transitions. For the sake of completeness, we also show in Tables II, IV, and VI some of the points taken from the binodal sections. The results we
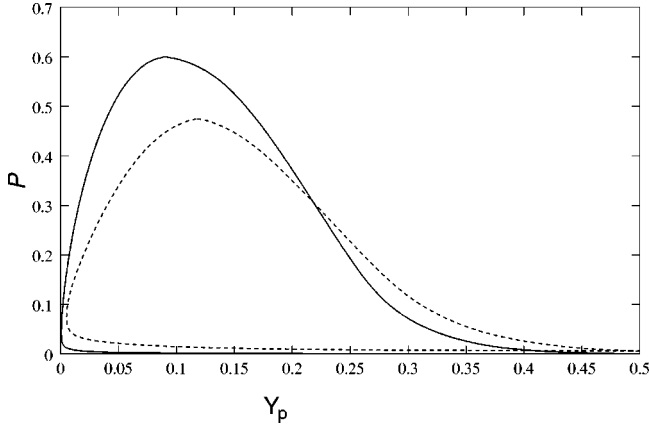
FIG. 3. Binodal section for $T=7.5$ (dashed line) and $T=5$ MeV (solid line) with the MS constants. The pressure is given in MeV/fm^3.

FIG. 4. Binodal section for $T=5$ MeV with the NL1 constants. The pressure is given in MeV/fm^3.

have chosen as input to the code which solves the differential equations (26)–(29) are displayed in the last three columns of these tables.

V. NUMERICAL RESULTS

Solving numerically the set of coupled equations (26)–(29) is not trivial. The main problem is related with the boundary conditions which have to be set within the droplet. To understand better this statement, we refer to [16], where the formulas are simplified to the $T=0$ case and this problem becomes clear. At first, we have tried to use the code
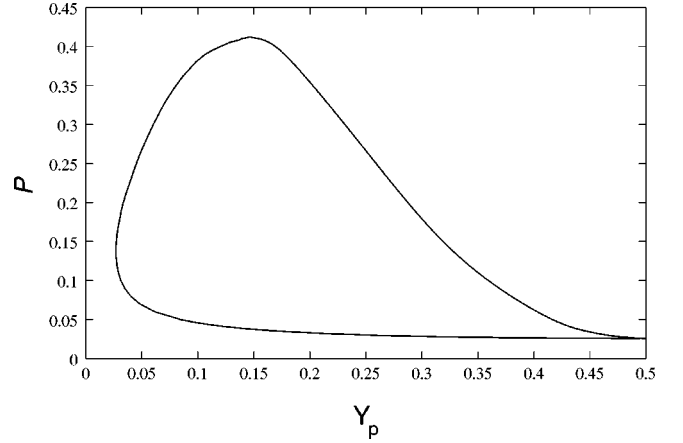
COLSYS [22], as suggested in [23] and [13], but we have obtained satisfactory results only for symmetric nuclear matter [24]. We have finally opted for another code, written with the help of the Gears stiff integration method, which uses as input the temperature, the size of the mesh, boundary conditions, and initial conditions. The chemical potentials are output and hence, obtained in accordance with the size of the mesh, R_{mesh}, which also determines the size of the droplet. The radius R_{mesh} fixes the neutron and proton chemical potentials and therefore, also the neutron and proton numbers. For details on the boundary conditions and trial functions for the meson and electromagnetic fields used in our code, we

TABLE II. Results obtained from the binodal section built with the MS constants for $T=7.5$ MeV. The fields are given in units of nucleon mass. In each row, the upper (lower) numbers represent the liquid (gas) phase.

Y_p	P (MeV/fm^3)	μ_p (MeV)	μ_n (MeV)	ρ_B (fm^{-3})	$\phi_0 \times 10^{-1}$	$V_{00} \times 10^{-1}$	$b_0 \times 10^{-2}$
0.28	0.15	879.373	940.061	0.14	0.352	0.232	-0.366
0.01				0.03	0.101	0.063	-0.202
0.30	0.11	881.589	938.792	0.15	0.361	0.239	-0.346
0.06				0.03	0.073	0.045	-0.145
0.33	0.07	885.506	936.607	0.16	0.376	0.249	-0.309
0.4×10^{-2}				0.01	0.040	0.024	-0.078
0.35	0.05	888.707	934.765	0.16	0.385	0.256	-0.279
0.5×10^{-2}				8.7×10^{-3}	0.026	0.016	-0.050
0.40	0.02	897.118	929.385	0.17	0.402	0.268	-0.196
0.01				3.3×10^{-3}	0.010	0.006	-0.019
0.45	0.01	905.860	922.798	0.18	0.413	0.275	-0.103
0.10				1.4×10^{-3}	0.004	0.003	-6.5×10^{-3}
0.48	0.007	910.560	918.704	0.18	0.415	0.276	-4.9×10^{-2}
0.26				9.7×10^{-4}	0.003	0.002	-2.7×10^{-4}
0.49	0.006	913.606	915.843	0.18	0.416	0.277	-0.014
0.43				8.7×10^{-4}	0.003	1.5×10^{-2}	-7.2×10^{-4}

TABLE III. Output results given by the solution of the coupled differential equations with the MS constants and $T=7.5$ MeV. Index i refers to $r=0$. The line with (*) is the output obtained from the conditions for $Y_p=0.4$ in Table II. (a) Output results given by the solution of the coupled differential equations with the MS constants and $T=7.5$ MeV without the inclusion of the electromagnetic field from the conditions for $Y_p=0.4$ in Table II.

$Y_p(i)$	μ_p (MeV)	μ_n (MeV)	σ (MeV fm^{-2})	t (fm)	R_{mesh} (fm)	R_p (fm)	Θ (fm)	$\rho_B(i)$ (fm^{-3})	Y
0.22	879.07	942.94	0.15	5.40	8.18	5.24	1.47	0.125	0.16
0.31	888.75	938.09	0.35	3.76	8.18	4.85	0.74	0.148	0.28
0.33	891.06	936.73	0.47	3.23	7.34	4.99	0.62	0.154	0.30
0.35	893.93	935.85	0.59	3.15	6.29	4.11	0.61	0.162	0.30
0.38	897.88	934.43	0.76	2.83	5.66	3.67	0.54	0.169	0.33
0.40	901.51	932.27	0.95	2.61	5.66	3.98	0.43	0.175	0.35
0.41	904.94	930.41	1.07	2.38	5.66	4.14	0.34	0.178	0.38
* 0.43	908.42	928.77	1.17	2.31	5.24	3.81	0.27	0.182	0.40
0.46	914.27	924.65	1.34	2.10	5.24	4.21	0.11	0.185	0.46
0.48	919.24	920.42	1.39	2.10	5.24	4.36	-0.02	0.186	0.52

(a)

$Y_p(i)$	μ_p (MeV)	μ_n (MeV)	σ (MeV fm^{-2})	t (fm)	R_{mesh} (fm)	R_p (fm)	Θ (fm)	$\rho_B(i)$ (fm^{-3})	Y
0.43	905.69	929.98	1.16	2.41	5.24	3.47	0.35	0.185	0.37

refer to [16]. We have assumed that convergence is achieved when the fields and baryonic density do not vary more than 10^{-3} from one run to the following one.

As an example, in Fig. 5 we plot the fields which are solutions of the coupled equations for the MS parametrization at $T=7.5$ MeV with the initial conditions given in Table II for $Y_p=0.4$ (solid lines). The corresponding baryonic density is plotted in Fig. 6 (top solid line) and represents a droplet of the liquid phase (small r) in the background of the vapor phase (large r). Similar density profiles are obtained for all other proton fractions.

Some quantities of interest to study the surface properties

TABLE IV. Results obtained from the binodal section built with the MS constants for $T=5$ MeV.

Y_p	P (MeV/fm^3)	μ_p (MeV)	μ_n (MeV)	ρ_B (fm^{-3})	$\phi_0 \times 10^{-2}$	$V_{00} \times 10^{-2}$	$b_0 \times 10^{-2}$
0.15	0.52	868.12	948.93	0.12	3.01	1.97	-0.48
0.05				0.09	2.28	1.48	-0.45
0.20	0.37	871.18	946.76	0.13	3.26	2.15	-0.46
0.02				0.07	1.92	1.23	-0.39
0.25	0.19	875.63	943.75	0.14	3.49	2.31	-0.41
6×10^{-3}				0.05	1.46	0.93	-0.30
0.30	0.06	881.47	940.25	0.15	3.73	2.47	-0.36
2×10^{-4}				0.02	0.62	0.38	-0.12
0.35	0.02	888.80	936.36	0.17	3.96	2.63	-0.29
2×10^{-4}				4×10^{-3}	0.13	0.08	-0.03
0.40	6×10^{-3}	897.55	930.92	0.18	4.12	2.74	-0.20
2×10^{-3}				1×10^{-3}	0.04	0.02	-0.01
0.45	1×10^{-3}	906.87	924.01	0.18	4.22	2.81	-0.10
0.03				3×10^{-4}	0.01	0.01	-2×10^{-3}
0.50	5×10^{-4}	915.82	915.89	0.18	4.25	2.83	0.0
0.50				1×10^{-4}	3×10^{-3}	2×10^{-3}	0.0

TABLE V. Output results given by the solution of the coupled differential equations with the MS constants and $T=5$ MeV.

$Y_p(i)$	μ_p (MeV)	μ_n (MeV)	σ (MeV fm^{-2})	t (fm)	R_{mesh} (fm)	R_p (fm)	Θ (fm)	$\rho_B(i)$ (fm^{-3})	Y
0.30	887.93	939.94	0.39	3.35	8.39	5.42	0.71	0.152	0.29
0.35	893.12	938.38	0.64	2.95	5.66	3.40	0.72	0.166	0.27
0.37	897.08	936.44	0.85	2.72	5.66	3.92	0.59	0.174	0.30
0.39	900.64	934.77	1.05	2.38	5.66	4.17	0.49	0.179	0.32
0.40	904.64	932.88	1.24	2.15	5.66	4.39	0.37	0.182	0.35
0.43	910.73	929.86	1.46	1.99	5.24	4.28	0.22	0.188	0.40
0.46	916.13	926.20	1.57	1.89	5.24	4.50	0.089	0.191	0.44
0.48	920.88	921.79	1.58	1.89	5.24	4.59	-0.03	0.191	0.49

are the two *squared-off* radii R_n and R_p in the spherical geometry, defined as

$$\int_0^{R'} \rho_n(r)r^2\,dr = \frac{1}{3}[\rho_{n,i}R_n^3 + \rho_{n,f}(R'^3 - R_n^3)], \quad (46)$$

and

$$\int_0^{R'} \rho_p(r)r^2\,dr = \frac{1}{3}[\rho_{p,i}R_p^3 + \rho_{p,f}(R'^3 - R_p^3)], \quad (47)$$

where ρ_i refers to the liquid density, ρ_f to the gas density, R' is larger than the size of the mesh and corresponds to the value of r where $|f(r) - f_g| < 10^{-8}$ with f being either a me-

son field or the baryonic density at r and f_g the corresponding gas value. Another important quantity is the thickness of the region at the surface with extra neutrons known as *neutron skin*. The *neutron skin thickness* is given by [15]

$$\Theta = R_n - R_p. \quad (48)$$

These quantities are computed for the droplet solutions we obtain and given in Tables III, V, and VII.

The droplet surface energy and thickness are obtained from the free energy of a system with a fixed number of particles $B = B_p + B_n$, in which a droplet of arbitrary size grows in the background of the vapor phase. The free energy reads

TABLE VI. Results obtained from the binodal section built with the NL1 constants for $T=5$ MeV.

| Y_p	P (MeV/fm^3)	μ_p (MeV)	μ_n (MeV)	ρ_B (fm^{-3})	$\phi_0 \times 10^{-2}$	$V_{00} \times 10^{-2}$	$b_0 \times 10^{-2}$
0.10	0.29	885.36	946.59	0.07	1.90	1.11	-0.35
0.11				0.06	1.82	1.06	-0.34
0.15	0.27	885.91	946.13	0.07	2.10	1.24	-0.35
0.07				0.05	1.61	0.92	-0.32
0.20	0.24	886.59	945.65	0.09	2.43	1.45	-0.35
0.06				0.05	1.51	0.86	-0.31
0.25	0.18	888.97	944.02	0.10	2.73	1.64	-0.33
0.03				0.04	1.23	0.69	-0.26
0.30	0.10	892.61	941.56	0.11	3.02	1.83	-0.30
0.01				0.03	0.85	0.47	-0.19
0.35	0.04	897.60	938.35	0.12	3.35	2.05	-0.25
3×10^{-3}				0.01	0.36	0.19	-0.08
0.40	0.01	904.32	933.97	0.13	3.67	2.26	-0.18
5×10^{-3}				3×10^{-3}	0.10	0.05	-0.02
0.45	4×10^{-3}	912.06	928.06	0.14	3.89	2.40	-0.10
0.05				8×10^{-4}	0.03	0.01	-5×10^{-3}
0.50	1.65×10^{-3}	920.42	920.46	0.14	3.97	2.45	-2×10^{-4}
0.50				3×10^{-4}	0.01	0.01	0.0
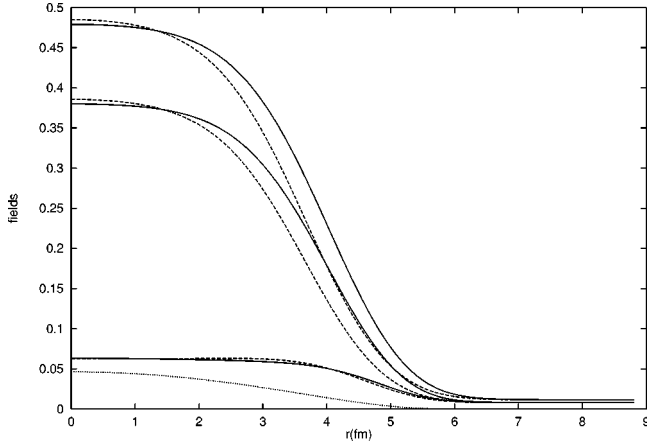
FIG. 5. From top to bottom the fields $g_s\phi$, g_vV_0, $g_\rho b_0(\times -5)$ (solid and dashed lines) and $eA_0(\times 10)$ (dotted line) are shown in terms of r. The fields are given in nucleon mass units and are obtained with the input values of Table II for $Y_p=0.4$. The solid curves were obtained with the inclusion of the electromagnetic field and the dashed ones without it.

$$F=\int 4\pi r^2 dr\left[\frac{1}{2}\left(\left(\frac{d\phi}{dr}\right)^2-\left(\frac{dV_0}{dr}\right)^2\right.\right.$$
$$\left.\left.-\left(\frac{db_0}{dr}\right)^2-\left(\frac{dA_0}{dr}\right)^2\right)-V_{ef}\right]+\mu_pB_p+\mu_nB_n, \quad (49)$$

where V_{ef} is given in Eq. (21). If the Coulomb field is neglected, F can be rewritten in the small surface thickness approximation as [12]

$$F=\int 4\pi r^2\,dr\left[\left(\frac{d\phi}{dr}\right)^2-\left(\frac{dV_0}{dr}\right)^2-\left(\frac{db_0}{dr}\right)^2-C\right]+\mu_pB_p$$
$$+\mu_nB_n, \quad (50)$$

where C is a constant. For droplets with radius R and volume V,

$$F(R)=4\pi\sigma R^2-CV+\mu_pB_p+\mu_nB_n. \quad (51)$$

The surface energy per unit area of these droplets in the small thickness approximation is

$$\sigma=\int_0^\infty dr\left[\left(\frac{d\phi}{dr}\right)^2-\left(\frac{dV_0}{dr}\right)^2-\left(\frac{db_0}{dr}\right)^2\right]. \quad (52)$$

When the Coulomb field is included, the small surface thickness approximation is not valid. However, as the electromagnetic interaction should not contribute to surface properties directly, we have considered the same definition for the surface energy and have defined the Coulomb energy as

$$E_c=\int 4\pi r^2\,dr\left[-\frac{1}{2}\left(\frac{dA_0}{dr}\right)^2+e\rho_pA_0\right]. \quad (53)$$

We have checked in [16], by means of a parametrization test, that the above approximation for the surface energy is a good one.
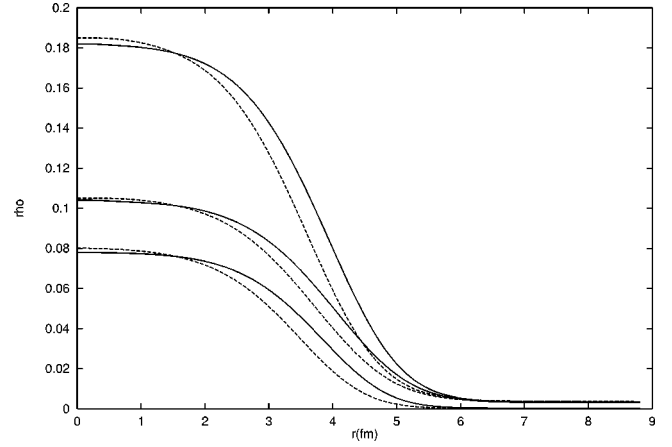

FIG. 6. From top to bottom the density profiles for the baryons $\rho_B(r)$, the neutrons $\rho_n(r)$ and the protons $\rho_p(r)$ in fm^{-3} are plotted for the same case as in Fig. 5. The solid curves were obtained with the inclusion of the electromagnetic field and the dashed ones without it.

The surface thickness t is defined as the width of the region where the density drops from $0.9\rho_{B0}$ to $0.1\rho_{B0}$, where ρ_{B0} is the baryonic density at $r=0$, after subtracting the background gas density.

In Table II some points taken from the binodal section for the MS constants at $T=7.5$ MeV are explicitly written. In Table III results found for the proton fractions at $r=0$ [$Y_p(i)$], chemical potentials,[1] the surface energy, its thickness, the size of the mesh for which convergence is achieved, R_{mesh}, R_p and the neutron skin thickness are displayed. Notice that there is a small discrepancy between the proton and neutron chemical potentials given in Table II and the ones displayed in Table III. This is due to finite size effects and the inclusion of the Coulomb interaction. In Tables IV and V again the points obtained from the binodal section at $T=5$ MeV and the respective droplet solutions are shown for the MS set of constants while in Tables VI and VII the NL1 constants are used.

We have also calculated, for every droplet shown in Tables III, V, and VII, the *proton fraction within the droplet* defined as

$$Y=\frac{Z}{Z+N},$$

where

$$N=B_n-B_{n\,gas}, \quad Z=B_p-B_{p\,gas},$$

are respectively the number of neutrons and protons in the droplet excluding the contribution from the background gas.

At this point some comments are in order. The size of the mesh (R_{mesh}) given in Tables III, V, and VII are the smaller

---

[1]In nonrelativistic models the chemical potential, μ_i', is related with the values given in the present work by $\mu_i'=\mu_i-M$, where $i=p,n$ and M is the nucleon mass.

TABLE VII. Output results given by the solution of the coupled differential equations with the NL1 constants and $T=5$ MeV.

$Y_p(i)$	μ_p (MeV)	μ_n (MeV)	σ (MeV fm^{-2})	t (fm)	R_{mesh} (fm)	R_p (fm)	Θ (fm)	$\rho_B(i)$ (fm^{-3})	Y
0.32	901.48	938.77	0.21	4.70	8.40	5.47	0.68	0.104	0.31
0.36	904.60	937.25	0.33	4.12	7.35	4.97	0.61	0.114	0.32
0.39	908.37	935.83	0.46	3.53	6.30	4.17	0.56	0.120	0.35
0.43	915.32	932.94	0.65	3.06	5.46	3.48	0.38	0.125	0.36
0.46	920.36	929.68	0.81	2.82	5.04	3.55	0.18	0.133	0.42
0.49	925.42	925.62	0.88	2.80	4.83	3.62	-0.01	0.136	0.49

values greater than 5 fm for which there is convergence for a given density at $r=0$ and a given proton fraction Y_p within the accuracy of the present numerical calculations. For the higher initial proton fractions $[Y_p(r=0)>0.4]$ and lower temperatures solutions corresponding to smaller droplets exist but in order to be possible a comparison of the data for two different temperatures we have opted for greater droplets. We have chosen to compare data corresponding to the same value of the proton fraction at $r=0$ because this parameter is independent of the properties of the surface. Before drawing our conclusions, we would like to emphasize that in our calculations, the proton and neutron numbers are never fixed. They are an output of the results for the fields and densities obtained from the convergent solutions of the differential equations.

VI. DISCUSSION OF THE RESULTS AND CONCLUSIONS

From Tables III, V, and VII, one can check that the surface energy σ increases with the initial proton fraction and its thickness t decreases. In fact, the larger the proton fraction the less important is the contribution from the b_0 field in the σ calculation as can be seen from Eq. (52). One can also see that the larger the liquid phase proton fraction, the smaller the size of the mesh for which convergence is achieved. This could be due to the decrease of neutron-proton asymmetry and therefore, the increase of the droplet binding.

In Tables III, V, and VII, the squared-off proton radius and the neutron skin thickness are also shown. One can observe that Θ decreases with the increase of Y for a fixed size of the mesh, so that droplets with a smaller percentage of protons inside present thicker neutron skins.

Some conclusions with respect to the temperature dependence of the droplet solutions can also be drawn comparing Tables III and V. The surface energy decreases with the increase of temperature, while the surface thickness is larger for higher temperatures. The decrease of σ with the temperature is easily understood from Eq. (52). In fact the main contribution for σ comes from the scalar field and for higher temperatures the fields decrease more smoothly and spread out over a larger distance at the surface and, therefore, their derivatives are smaller. The neutron skin thickness is a quantity which is larger for lower temperatures. For results at zero temperature, please refer to [16].

Next, we examine the behavior of the total baryonic den-

sity. In Fig. 6 the baryonic, neutron, and proton densities are plotted from top to bottom for the MS parametrization, $T=7.5$ MeV and the boundary conditions corresponding to the $Y_p=0.4$ entrance in Table II. The solid lines include the Coulomb interaction and the dashed lines were obtained with the Coulomb interaction switched off. The baryonic density falls from the initial liquid density to the vapor density, which is different from zero, as expected. Concerning the neutron and proton densities, Fig. 6 shows the same profile obtained with nonrelativistic models.

Except for the symmetric nuclear matter, the proton fraction in the vapor phase is smaller than in the liquid phase $[Y_p(i)]$. This can be seen from Tables II, IV, and VI and confirmed for the droplet solutions. This fact can be interpreted as a droplet with a given proton concentration (the phase of higher density) in equilibrium with a gas of drip nucleons, mostly neutrons (the lower density phase) with a much smaller proton concentration.

Concerning the importance of the Coulomb interaction and its consequences in the droplet formation, one can see, from Fig. 6, that the proton and neutron densities are indeed modified by the electromagnetic field, as pointed out in [1]. The effect of the electromagnetic field is to decrease the number of particles in the droplet, since the central density becomes smaller, and to spread out the distribution of the nucleons, namely the protons. Figures 5 and 6 correspond to the values shown on the seventh line of Table III (marked with an asterisk) and Table III(a), respectively with and without the electromagnetic field. The surface energy stays almost unaffected while the surface thickness, the neutron thickness, and the central density decrease with the inclusion of the Coulomb field and the proton radius increases.

For liquid proton fractions smaller than the ones shown in Tables III, V, and VII, the program does not converge, and a more careful numerical analysis is needed in this region in order to determine the smallest proton fraction for which droplets still exist. This behavior is also a consequence of the electromagnetic interaction. If it is not considered, droplets with fields and densities similar to the ones encountered in the binodal section at $r=0$ and $r=R_{\text{mesh}}$ are obtained.

The conclusions drawn above are independent of the sets of parameters used. Comparing the results obtained for the two sets of parameters we conclude that the MS parametrization corresponds to a harder equation of state and, therefore, the central densities and surface energy are much higher

while the surface and neutron thicknesses are smaller than the values obtained for the same quantities with the NL1 parametrization.

In summary, we have studied the surface properties of arising droplets in a vapor system under conditions predetermined by the binodal section obtained in situations where two-phase coexistence is possible for certain fixed temperatures. The droplets are described in terms of the extended Walecka model within the Thomas-Fermi approximation. To the best of our knowledge, this is the first time that the electromagnetic interaction is taken into account within the framework of a relativistic model in order to calculate surface properties for droplets at finite temperatures. We believe that a more systematic study of the importance of the Coulomb field for various temperatures and proton fractions has still to be made. The properties calculated in the present paper are important, for instance, in the study of the phase boundary between the liquid matter of the interior of a neu-

tron star and the matter that comprises its crust. In this case we have protons, neutrons, and electrons in beta equilibrium. These problems will be tackled in a forthcoming work.

---

[1] P. Bonche, S. Levit, and D. Vautherin, Nucl. Phys. **A427**, 278 (1984); **A436**, 265 (1985).

[2] H. Müller and B. D. Serot, Phys. Rev. C **52**, 2072 (1995).

[3] H. Reinhardt and H. Schulz, Nucl. Phys. **A432**, 630 (1985).

[4] A. H. Blin, B. Hiller, H. Reinhardt, and P. Schuck, Nucl. Phys. **A484**, 295 (1988).

[5] S. L. Shapiro and S. A. Teukolsky, *Black Holes, White Dwarfs and Neutron Stars* (Wiley, New York, 1983); C. J. Pethick, D. G. Ravenhall, and C. P. Lorenz, Nucl. Phys. **A584**, 675 (1995).

[6] D. G. Ravenhall, C. J. Pethick, and J. M. Lattimer, Nucl. Phys. **A407**, 571 (1983); G. Baym, H. A. Bethe, and C. J. Pethick, *ibid.* **A175**, 225 (1971); D. G. Ravenhall, C. D. Bennet, and C. J. Pethick, Phys. Rev. Lett. **28**, 978 (1972).

[7] A. L. Goodman, J. I. Kapusta, and A. Z. Mekjian, Phys. Rev. C **30**, 851 (1984).

[8] K. Kolehmainen, M. Prakash, J. M. Lattimer, and J. R. Treiner, Nucl. Phys. **A439**, 535 (1985).

[9] W. D. Myers, W. J. Swiatecki, and C. S. Wang, Nucl. Phys. **A436**, 185 (1985).

[10] E. Suraud, Nucl. Phys. **A462**, 109 (1987).

[11] F. J. B. Salzedas, MSc. dissertation, Universidade de Coimbra, 1995.

[12] M. Nielsen and J. Providência, J. Phys. G **16**, 649 (1990).

[13] H. Müller and R. M. Dreizler, Nucl. Phys. **A563**, 649 (1993).

[14] D. Von Eiff, J. M. Pearson, W. Stocker, and M. K. Weigel, Phys. Lett. B **324**, 279 (1994).

[15] M. Centelles, M. Del Estal, and X. Viñas, Nucl. Phys. **A635**, 193 (1998).

[16] D.P. Menezes and C. Providência, Nucl. Phys. **A650**, 283 (1999).

[17] J. Boguta and A. R. Bodmer, Nucl. Phys. **A292**, 413 (1977); A. R. Bodmer and C. E. Price, *ibid.* **A505**, 123 (1989); A. R. Bodmer, *ibid.* **A526**, 703 (1991).

[18] Y. K. Gambir, P. Ring, and A. Thimet, Ann. Phys. (N.Y.) **198**, 132 (1990); H. Berghammer, D. Vretenar, and P. Ring, Phys. Lett. B **296**, 290 (1992); D. Vretenar, H. Berghammer, and P. Ring, *ibid.* **319**, 29 (1993); H. Berghammer, D. Vretenar, and P. Ring, Nucl. Phys. **A560**, 1014 (1993).

[19] K. Sumiyoshi and H. Toki, Astrophys. J. **422**, 700 (1994).

[20] B. D. Serot and J. D. Walecka, Adv. Nucl. Phys. **16**, 1 (1995).

[21] M. Barranco and J. R. Buchler, Phys. Rev. C **22**, 1729 (1980).

[22] U. Asher, J. Christiansen, and R. D. Russell, Math. Comput. **33**, 659 (1979); U. Asher, J. Comput. Phys. **34**, 401 (1980); G. Bader and U. Asher, SIAM (Soc. Ind. Appl. Math.) J. Sci. Stat. Comput. **8**, 483 (1987).

[23] C. Speicher, E. Engel, and R. M. Dreizler, Nucl. Phys. **A562**, 569 (1993).

[24] M. Centelles, X. Viñas, M. Barranco, S. Marcos, and R. J. Lombard, Nucl. Phys. **A537**, 486 (1992).